Dalton Transactions

ROYAL SOCIETY OF CHEMISTRY

PAPER

View Article Online
View Journal | View Issue

Cite this: *Dalton Trans.*, 2024, **53**, 15481

Enhancing lithium storage performance with silicon-based anodes: a theoretical study on transition metal-integrated SiO_x/M@C (M = Fe, Co, Ni) heterostructures†

Mianying Huang, ‡[a] Yueying Chen,‡[a] Wenhai Zeng,[b] Yiqing Liu,[a] Zhiguang Xu, *[a] Yongbo Wu,[c,d] Xiaoming Lin *[a] and Xuan Xu[a]

Received 2nd August 2024,
Accepted 2nd September 2024

DOI: 10.1039/d4dt02205j

rsc.li/dalton

In lithium-ion batteries, infusible metals with lithium, such as Mg, Fe, Co, Ni, and Cu are often utilized. However, current research predominantly focuses on the experimental aspects of the (de)lithiation process, with limited exploration from a theoretical calculation perspective. The extensive use of experimental methods to study the many electrochemically inert metals is time-consuming and costly. In this study, we successfully constructed and optimized SiO_x/M@C (M = Fe, Co, Ni) heterostructures, integrating transition metal nanoparticles to address the electrochemical inertness and slow diffusion kinetics of pristine SiO_x. A comprehensive density functional theory (DFT) study was conducted to examine the effects of different metal heterostructures on the structural, migration potential energy, and adsorption properties during lithium-ion intercalation. The results demonstrate that the SiO_x/Fe@C heterostructure exhibits the lowest migration energy barrier, significantly enhancing lithium-ion transport compared to SiO_x/Co@C and SiO_x/Ni@C. Consequently, the SiO_x/Fe@C electrode shows superior high-rate discharge capability and excellent cycling performance through electrochemical measurements. Additionally, the study delves into the intrinsic mechanisms through charge density differences and Fermi level calculations, providing valuable insights into the importance of hybrid strategies for incorporating inert metals into anode materials for lithium-ion batteries.

Introduction

With the growing development and utilization of energy, issues such as resource depletion and environmental pollution are becoming increasingly critical. There is an urgent need for clean, sustainable, and efficient energy sources such as wind and solar power.[1,2] Concurrently, the economic growth has led to an increase in automobile usage, which has emerged as a significant contributor to global greenhouse gas emissions. Consequently, the advancement of clean energy for electric vehicle propulsion is critical for achieving carbon neutrality.[3,4] Nevertheless, the intermittent nature of wind and solar energy necessitates the development of advanced energy storage systems capable of efficiently storing electricity generated from these renewable sources.[5,6] Lithium-ion batteries have garnered significant research attention for electric vehicle applications due to their environmental benefits, high energy density, long cycle life, and commercial viability.[7,8] However, the current graphite electrodes used as anode materials fall short of meeting the demands of high-performance electric vehicles, owing to their low theoretical capacity (372 mA h g^{-1}), lithiation voltage near the Li^+ potential (0 V *vs.* Li^+/Li), and limited cycle life.[9–13] Consequently, there is an urgent need to develop novel anode materials with enhanced capacity to augment the storage capability of these batteries.

Currently, three primary reaction mechanisms for anode materials have been reported: intercalation, alloying, and conversion.[14,15] Among these, alloying anode materials, particularly silicon, exhibit an exceptionally high theoretical lithium storage capacity of 4200 mA h g^{-1}, approximately 11 times greater than that of graphite.[16–19] However, the signifi-

[a]*Key Laboratory of Theoretical Chemistry of Environment, Ministry of Education, School of Chemistry, South China Normal University, Guangzhou 510006, China. E-mail: chzgxu@scnu.edu.cn, linxm@scnu.edu.cn*
[b]*College of City Construction, Jiangxi Normal University, Nanchang 330022, P. R. China*
[c]*Key Laboratory of Atomic and Subatomic Structure and Quantum Control (Ministry of Education), Guangdong Basic Research Center of Excellence for Structure and Fundamental Interactions of Matter, School of Physics, South China Normal University, Guangzhou 510006, China*
[d]*Guangdong Provincial Key Laboratory of Quantum Engineering and Quantum Materials, Guangdong-Hong Kong Joint Laboratory of Quantum Matter, South China Normal University, Guangzhou 510006, China*

†Electronic supplementary information (ESI) available. See DOI: https://doi.org/10.1039/d4dt02205j

‡These authors contributed equally to this work.

cant volume changes and inadequate ion diffusion kinetics of crystalline silicon during cycling pose substantial barriers to its further commercialization.[20–24] In contrast to crystalline silicon, SiO_x ($0 < x < 2$) electrodes present advantages such as lower cost and reduced volume expansion, positioning them as promising candidates to advance silicon-based anode materials.[25–28] Notably, SiO_x-based anodes generate Li_2O and Li_4SiO_4 *in situ* during the lithiation process, which aids in the formation of a stable solid electrolyte interface (SEI) layer and mitigates the volume change of SiO_x.[29–32] However, the volume expansion of silicon oxide is still significant and does not meet the requirements of lithium-ion batteries. The high binding energy of Si–O bonds and the formation of inactive products like Li_2O and Li_4SiO_4 contribute to a low initial coulombic efficiency (ICE).[33–35] Additionally, the inherent low electronic conductivity of silicon oxide results in poor electrochemical kinetics and cycling stability, impeding the further development and application of SiO_x electrodes.[36,37]

To address these challenges, extensive research efforts have been undertaken to enhance the capacity, conductivity, ICE, and cycling performance of SiO_x anodes.[38] One approach involves the construction of SiO_x/C composites by integrating SiO_x with conductive carbon.[25,31,39,40] For instance, Liu *et al.* synthesized SiO_x/C microspheres, significantly improving the electronic conductivity of SiO_x, achieving a specific capacity of 689 mA h g^{-1} at 500 mA g^{-1} and a capacity retention rate of 91.0% after 400 cycles.[37] Xiong *et al.* engineered an anode composed of a nitrogen and cobalt-doped carbon shell surrounding a silicon heterostructure, which demonstrated outstanding electrochemical performance, retaining a coulombic efficiency exceeding 97% after 500 cycles.[41] Ji *et al.* developed SiO anode materials by incorporating a carbon coating and lithium hydride, which resulted in improved cycling performance due to the protective carbon layer.[42] The incorporation of carbon not only enhances the electrode's conductivity but also mitigates the volume expansion of SiO_x during cycling, thereby improving cycling stability.[43–45] Another strategy entails the introduction of transition metals (*e.g.*, Cu, Fe, Co, Ni) with high conductivity to construct SiO_x composites.[46,47] Shen *et al.* demonstrated an exceptionally high capacity of 932 mA h g^{-1} and excellent cycling stability over more than 1000 cycles in lithium-ion batteries by synthesizing novel hierarchical hollow SiO_2 spheres modified with metal Co nanoparticles.[33] Zhong *et al.* incorporated cobalt into SiO_2 to address the challenges of limited conductivity and significant volume expansion associated with SiO_2.[48]

Utilizing the synergistic benefits of alloying and carbon material integration strategies, we have successfully synthesized stacked SiO_x/Co@C composites, modified with Co nanoparticles.[49] This composite demonstrated a high reversible capacity of 815.5 mA h g^{-1} after 240 cycles.[49] The formation of a heterogeneous structure and the incorporation of Co metal catalyzed the conversion of Si–O bonds, thereby enhancing electrochemical reversibility and accelerating reaction kinetics.[33,50] These findings indicate that electrochemically inert metals can significantly improve the structural stability of electrode materials while mitigating volume expansion.[49] However, in addition to Co, infusible metals with lithium, such as Mg, Fe, Ni, and Cu, also warrant thorough investigation to elucidate their underlying mechanisms.[46] A comprehensive atomic-level understanding of the interfacial regions and the impact of metal interface charge transfer on silicon oxide systems remains elusive, which is vital for the design of silicon oxide electrodes. Transition metals like Fe, Co, and Ni are commonly employed to form heterostructures with SiO_x, enhancing the electrochemical performance of lithium-ion anode materials.[51–54] However, most studies on silicon oxide electrodes focus on the electrochemical mechanisms of the (de)lithiation process from an experimental perspective, with limited exploration of lithium-ion battery mechanisms through theoretical calculations. The extensive use of experimental methods to study the many electrochemically inert metals is time-consuming and costly. Our previous research employed density functional theory (DFT) calculations to investigate the impact of metal/non-metal heterostructures on Co_2VO_4 electrode materials, considering migration energy barriers, adsorption energies, and density of states, with theoretical results aligning with experimental findings.[55] Additionally, we demonstrated the effect of Sb–O–C bonds in Sb/C materials by calculating lithium-ion migration energy barriers, showing a significant reduction in migration energy barriers.[56] These findings illustrate that DFT calculations can successfully interpret and predict various experimental outcomes.[57–60]

In this study, we employed density functional theory (DFT) calculations to construct and optimize SiO_x/M@C (M = Fe, Co, Ni) heterogeneous structures. We calculated lithium-ion migration potential, lithium-ion adsorption energy, differential charge density, and Fermi level to explore the impact of Fe, Co, and Ni on the SiO_x@C anode materials and analyse the charge transfer characteristics between the metal and graphite or silicon oxide interfaces. Relevant experiments were conducted, and the experimental findings were consistent with the theoretical calculations. Our research provides a theoretical foundation for the design of advanced silicon oxide materials and offers insights into the hybrid strategy of incorporating inert metals for application in lithium-ion battery anode materials.

Experimental section

DFT calculation approach

The computations were performed using the CASTEP program within Materials Studio. The electron interaction energy of exchange–correlation was defined using the generalized gradient approximation (GGA) with the Perdew–Burke–Ernzerhof (PBE) functional. A plane wave cutoff energy of 450 eV was employed for all calculations. The first Brillouin zone was sampled using a $3 \times 3 \times 1$ *k*-point grid following the Monkhorst–Pack scheme. The energy convergence criteria were set at 2×10^{-6} eV, and the geometry optimization convergence was set at 2×10^{-5} eV. Migration paths and energy bar-

riers were predicted using the linear synchronous transition (LST) and/or quadratic synchronous transition (QST) methods.[61]

Material characterization

Synthesis of SiO_x/M@C (M = Fe, Co, Ni). Silane/MOF precursors were synthesized through a straightforward electrostatic attraction method. Initially, 3.2 g of terephthalic acid (BDC) was dissolved in a solution composed of 120 mL of deionized water and 20 mL of *N*,*N*-dimethylformamide (DMF) in a water bath at 80 °C. After stirring for 1 hour, APTES was gradually added to the homogeneous solution, followed by an additional hour of stirring in the water bath. Subsequently, ferric nitrate or cobalt nitrate, or nickel nitrate were introduced, and the reaction mixture was stirred for another hour. Upon natural cooling to room temperature, the resulting precipitate was centrifuged and washed three times with both deionized water and ethanol. The final product, a silane/M-BDC (M = Fe, Co, Ni) precursor, was obtained after vacuum drying at 60 °C for 24 hours. To prepare SiO_x/M@C (M = Fe, Co, Ni) loaded with metal, the synthesized silane/M-BDC (M = Fe, Co, Ni) powder was pyrolyzed at 1000 °C under a nitrogen atmosphere for 3 hours at a heating rate of 5 °C min^{-1}.

Electrochemical measurements

The working electrode was prepared using a mass ratio of 70 : 15 : 15 for the active material, sodium alginate, and Super P, respectively. These components were thoroughly mixed with deionized water in a mortar and vigorously stirred for 12 hours. The resulting slurry was then uniformly cast onto copper foil and subjected to overnight vacuum drying at 90 °C. The average mass loading of the active material on the electrode was approximately 0.77 mg cm^{-2}. For electrochemical tests of half cells, the specific capacity was calculated based on the mass of the active material. Half-cell testing was conducted using a CR2032 coin cell configuration, with a pure lithium disc serving as the counter-electrode. Assembly took place in an argon-filled glove box ($H_2O \leq 0.1$ ppm, $O_2 \leq 0.1$ ppm). The electrolyte comprised 1 M $LiPF_6$ dissolved in a 1 : 1 : 1 volume ratio mixture of ethylene carbonate (EC), diethyl carbonate (DEC), and ethyl methyl carbonate (EMC). Celgard 2400 membrane was used as the separator. The LAND CT2001A battery test system was employed to evaluate lithium storage performance at room temperature, across various current densities within a voltage range of 0.01–3.00 V. Cyclic voltammetry (CV) was conducted using the CHI760E electrochemical workstation, with scans performed at different rates and impedance measurements taken over frequencies ranging from 100 kHz to 0.1 Hz.

Results and discussion

Crystal structure

To construct the heterostructures of SiO_2 and graphene layers, SiO_2 with a *P*3121 space group and graphene with a *P*63/*mmc* space group were selected. To accurately build the model, an interface supercell was used to minimize lattice mismatch and achieve relatively low strain. Consequently, the SiO_x@C structure is composed of (2 × 2) SiO_2 and (4 × 4) graphene layers, as depicted in Fig. S1,† with a lattice mismatch rate of 0.142%, indicating model accuracy. The unit cell dimensions are 9.82600 × 9.82600 × 25.0000 Å, with the addition of a 11 Å vacuum layer.

According to our previous research, the (111) facets of transition metals Fe, Co, and Ni are easily exposed to air, facilitating interface formation.[55,62,63] Thus, in constructing the SiO_x@C electrode heterostructure, the (111) planes of Fe, Co, and Ni were primarily studied. The space group for the metal structures is *P*63/*mmc*. After optimizing the relaxation of the unit cell, the Fe(111), Co(111), and Ni(111) crystal planes were established and combined with SiO_x@C to form heterogeneous interfaces, as illustrated in Fig. 1. The formation energy of M in SiO_x/M@C was calculated using the following formula:

$$\Delta E_f = E(SiO_x/M@C) - E(SiO_x@C) - E(M) \quad (1)$$

where $E(SiO_x/M@C)$is the total energy of SiO_x/M@C (M = Fe, Co, Ni), $E(SiO_x@C)$ is the total energy of SiO_x, and $E(M)$ is the total energy of the metal. The calculated adsorption energies are presented in Table S1,† with the values of $E(SiO_x/M@C)$, $E(SiO_x@C)$, and $E(M)$ provided therein. The formation energies of the metals in SiO_x/Fe@C, SiO_x/Co@C, and SiO_x/Ni@C are 15.718 eV, 4.388 eV, and 3.288 eV, respectively. These indicate that combining SiO_x with these metals requires energy, with SiO_x/Fe@C requiring the most energy, followed by SiO_x/Co@C, which is close to SiO_x/Ni@C.

Moreover, as depicted in Fig. 1a–c, the minimum vertical separations between the carbon layer and the metal atoms Fe, Co, and Ni are 3.986 Å, 4.286 Å, and 4.786 Å, respectively, while the corresponding distances between the SiO_x layer and these metals are 5.003 Å, 4.151 Å, and 4.398 Å. Notably, the van der Waals radii for carbon, Fe, Co, Ni, and Si are 2.04 Å, 2.23 Å, 2.23 Å, 2.22 Å, and 2.29 Å, respectively, indicating that these interlayer distances are nearly equivalent to the sum of the van der Waals radii of the respective atoms.[64] This observation suggests that the interactions between the carbon and metal layers, as well as between the metal layers and the SiO_x layer, are primarily governed by van der Waals forces.

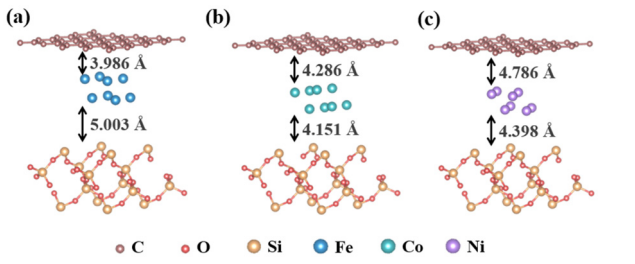

Fig. 1 Geometrically optimized structures of (a) SiO_x/Fe@C; (b) SiO_x/Co@C; (c) SiO_x/Ni@C.

Migration barriers

To accurately compare the influence of different metals on the silica electrode, four silicon atoms on the surface of SiO_2 were identified as the primary adsorption sites. These sites were designated as Si_I, Si_{II}, Si_{III}, and Si_{IV} in a clockwise sequence, with the corresponding metal sites labeled as M_I, M_{II}, M_{III}, and M_{IV}. Lithium-ion adsorption was subsequently performed based on these sites, with the positions before and after adsorption depicted in Fig. S2–4.†

Based on our previous studies and literature reports, the activation mechanism of SiO_x materials during lithium intercalation and lithium-ion extraction can be speculated as follows:

$$SiO_x + 2xLi^+ + 2xe^- \rightarrow xLi_2O + Si \quad (2a)$$

$$4SiO_x + 4xLi^+ + 4xe^- \rightarrow xLi_4SiO_4 + (4-x)Si \quad (2b)$$

$$5SiO_x + 2xLi^+ + 2xe^- \leftrightarrow xLi_2Si_2O_5 + (5-2x)Si \quad (2c)$$

$$Si + xLi^+ + xe^- \leftrightarrow Li_xSi\ (x \leq 4.4) \quad (2d)$$

$$MO + 2Li^+ + 2e^- \leftrightarrow M + Li_2O \quad (2e)$$

Based on the structural characteristics and reaction processes, the bottom of graphene and the middle of SiO_x were selected as the starting and ending points for lithium-ion migration. Four optimal adsorption sites were identified and optimized along the directions of the metal and Si to serve as pathway points for the migration path. These pathway sites are depicted in Fig. 2a, where Li_C represents the adsorption site below the graphene (starting point), and Li_{MID} represents the adsorption site in the middle of the SiO_x (ending point). As shown in Fig. 2b, Li_{Fe_I}, $Li_{Fe_{II}}$, $Li_{Fe_{III}}$, and $Li_{Fe_{IV}}$ represent the optimal adsorption sites of Li in four directions around the metal Fe. Similarly, the optimal adsorption sites for Li around the metals cobalt or nickel are indicated by corresponding symbols. Fig. 2c illustrates the optimal adsorption sites for lithium ions on SiO_x in different materials, using the Si position as the reference point, represented by Li_{Si_I}, $Li_{Si_{II}}$, $Li_{Si_{III}}$, and $Li_{Si_{IV}}$. From these sites, migration energy barriers were calculated for three segments: from the starting point to the metal (Path 1), from the metal to Si (Path 2), and from Si into the SiO_x (Path 3). This allowed for a comparative analysis of diffusion properties across different directions and materials. Based on this approach, the initiation and termination points of lithium-ion migration for each path were identified. By utilizing Reaction Preview, atomic pairings were established, and the migration paths were segmented into discrete fragments according to the applied computational methodology. Energy evaluations were then conducted in proximity to each frag-

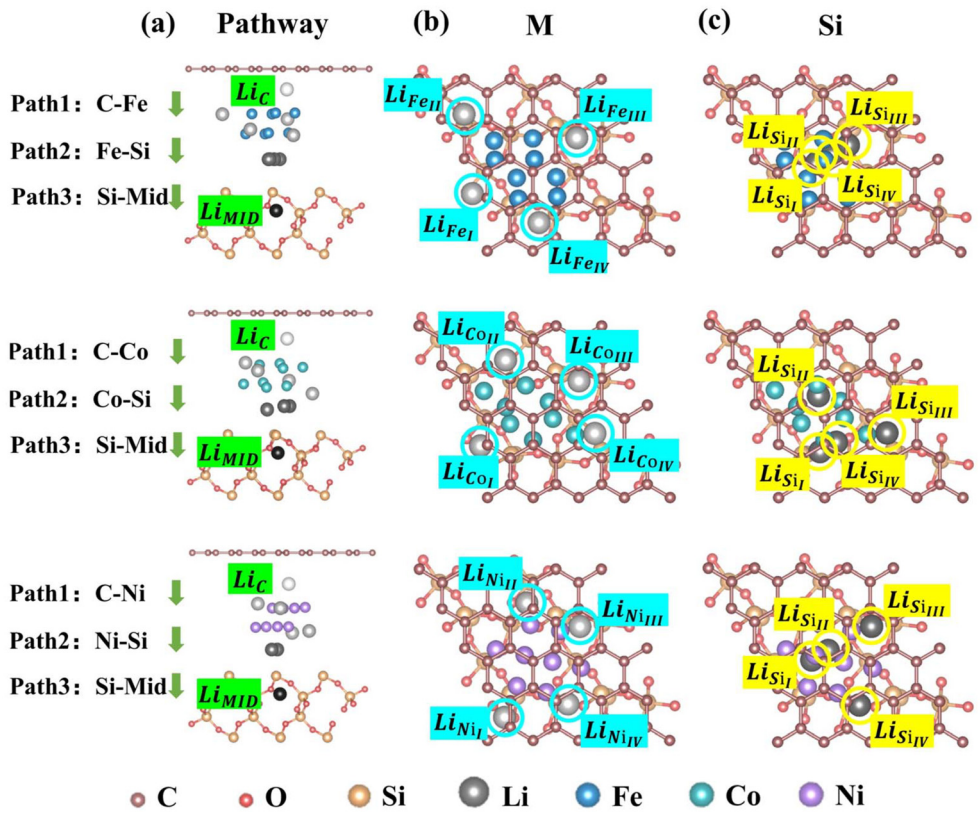

Fig. 2 (a) Schematic diagram of SiO_x/M@C (M = Fe, Co, Ni) for Path 1, Path 2, Path 3; (b) the optimized schematic diagram of lithium ions in SiO_x/M@C (M = Fe, Co, Ni) in the direction M_I, M_{II}, M_{III}, and M_{IV}; (c) the optimized schematic diagram of lithium ions in SiO_x/M@C (M = Fe, Co, Ni) in the direction Si_I, Si_{II}, Si_{III}, and Si_{IV}.

ment, enabling the quantification of the energy barriers associated with the migration process. Subsequently, three consecutive migration pathways in four distinct directions were computed for each material, and the corresponding energy distributions for these pathways were plotted collectively, as illustrated in Fig. 3–5. As depicted in the individual path diagrams (Fig. 3–5), lithium ions must overcome the forces exerted by the first and second layers of metal before traversing the oxygen site in silicon and successfully entering the SiO_x, where they combine with more silicon. The transition state during migration corresponds to the highest point in the energy profile, representing the critical energy barrier that must be overcome. In each migration energy barrier diagram, the first energy peak indicates the transition state near the first metal layer, signifying that lithium ions must overcome this initial barrier to proceed with migration. Similarly, the second energy peak corresponds to the transition state near the second metal layer, requiring the lithium ions to surmount the second metal barrier. Upon overcoming the metal-induced obstacles and entering Path 3, the third energy peak arises, with the transition state positioned near the surface oxygen atoms of SiO_x. At this stage, the lithium ions must overcome the force exerted by the oxygen atoms to enter the SiO_x structure for the subsequent reaction.

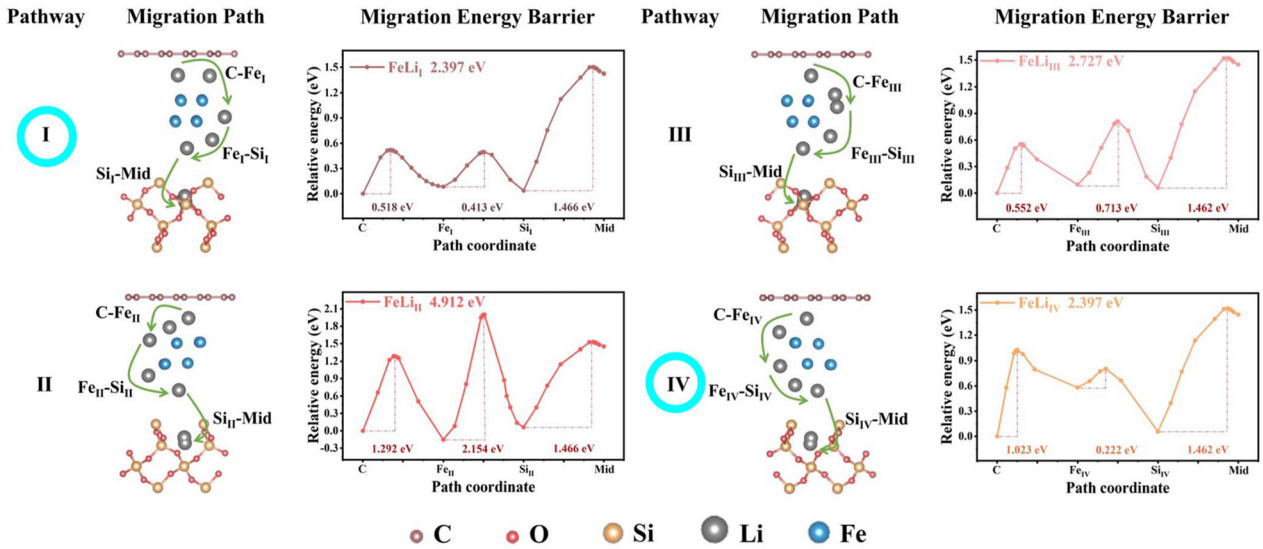

Fig. 3 Migration paths and energy barriers of lithium-ion in SiO_x/Fe@C in directions I, II, III, and IV.

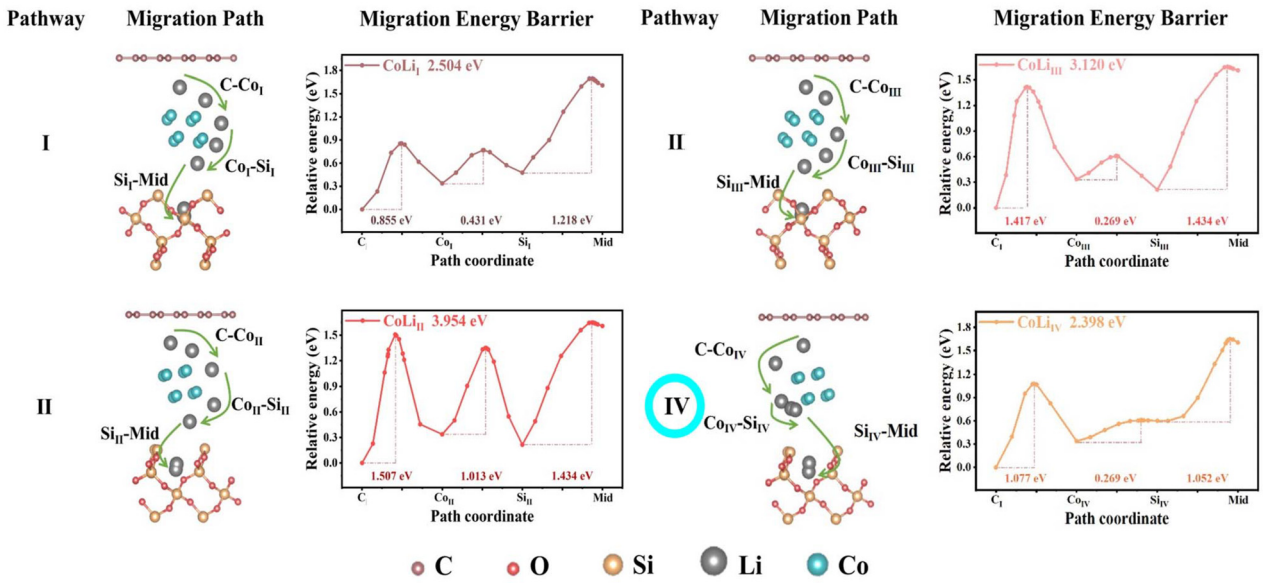

Fig. 4 Migration paths and energy barriers of lithium-ion in SiO_x/Co@C in directions I, II, III, and IV.

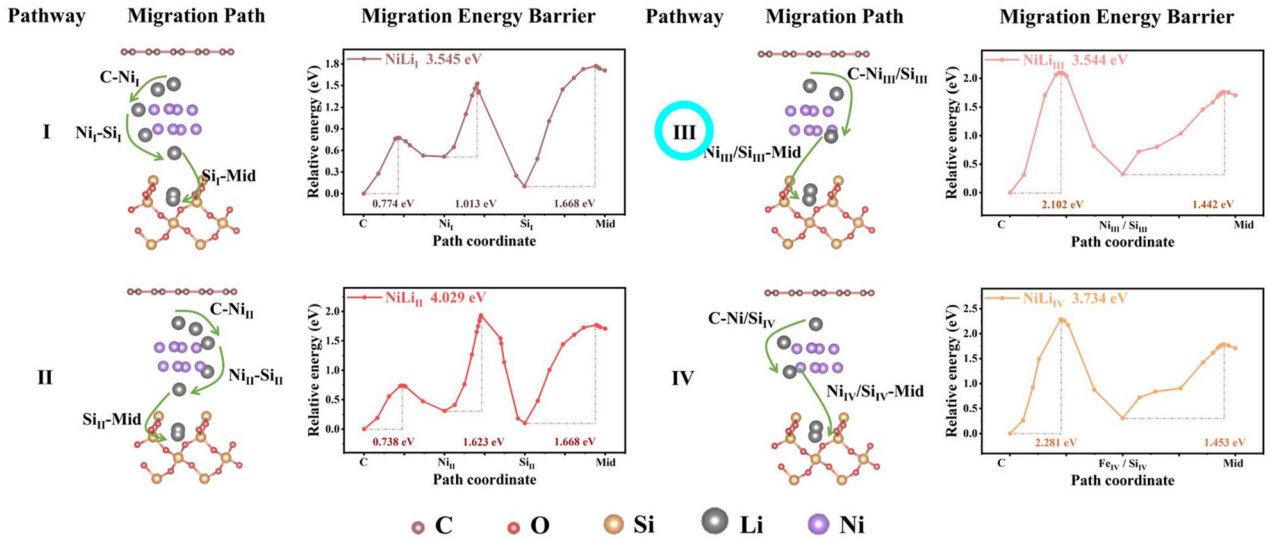

Fig. 5 Migration paths and energy barriers of lithium-ion in SiO_x/Ni@C in directions I, II, III, and IV.

As illustrated in Fig. 3, in SiO_x/Fe@C, the energy barrier for lithium ions migrating through direction II is significantly higher than that of the other three directions. Consequently, according to kinetic principles, lithium ions predominantly migrate *via* directions I, III, and IV, with an average energy barrier of 2.504 eV. Among these, directions I and IV are identified as the most favorable migration pathways. Notably, when lithium ions transition from Si into in SiO_x (*i.e.*, Path 3), the migration energies required for all directions are nearly identical. This indicates that the process of lithium ions entering silicon oxide in SiO_x/Fe@C is highly stable, allowing for uniform combination with silicon from all directions. This uniformity facilitates strong conductivity and a rapid lithium-ion shuttle rate.

As shown in Fig. 4, the average energy barrier for lithium ions in SiO_x/Co@C is 2.994 eV, with direction IV identified as the optimal migration pathway. Compared to SiO_x/Fe@C, the energy barrier for lithium ions in SiO_x/Co@C is higher, particularly from the starting point to the metal (*i.e.*, Path 1), which negatively impacts the subsequent migration efficiency of lithium ions in SiO_x/Co@C. In SiO_x/Ni@C (Fig. 5), the average energy barrier for lithium ions is 3.713 eV, with direction III being the most favorable migration pathway. Directions III and IV share the same optimal adsorption site near the metal and Si, necessitating only two migration paths for lithium ions to enter the SiO_x.

Therefore, based on the average energy barriers of the three materials, it is evident that lithium ions require the least energy in SiO_x/Fe@C, followed by SiO_x/Co@C, with SiO_x/Ni@C having the highest energy requirement. This pattern is consistent when comparing the optimal pathways for lithium-ion migration. In the case of SiO_x/Fe@C, two optimal migration paths for lithium ions were identified, designated as direction I and path IV, each necessitating a migration energy barrier of 2.397 eV. Conversely, SiO_x/Co@C and SiO_x/Ni@C each exhibit a single optimal lithium-ion migration path, with energy barriers of 2.398 eV and 3.544 eV, respectively. Consequently, SiO_x/Fe@C demonstrates superiority among the three materials, both in terms of the number of optimal migration paths and the associated energy barriers.

As depicted in Fig. 1–3, the average energy barriers for lithium ions traversing path 1 in different directions are 0.698 eV for SiO_x/Fe@C, 1.214 eV for SiO_x/Co@C, and 1.474 eV for SiO_x/Ni@C. For path 2, the energy barriers are 0.449 eV for SiO_x/Fe@C, 0.496 eV for SiO_x/Co@C, and 1.383 eV for SiO_x/Ni@C. Path 3 requires energy barriers of 1.463 eV for SiO_x/Fe@C, 1.285 eV for SiO_x/Co@C, and 1.558 eV for SiO_x/Ni@C. Consequently, for path 1, SiO_x/Fe@C exhibits a significantly lower energy barrier compared to the other two materials, facilitating a higher passage of lithium ions through path 1 and enabling subsequent migration to quickly reach the silicon oxide for the next reaction. In contrast, SiO_x/Ni@C displays higher average migration energy barriers for lithium ions across all three paths, resulting in a reduced migration rate of lithium ions.

As a result, from the perspective of migration energy barriers, it is evident that the energy barrier for lithium-ion migration in SiO_x/Fe@C is the lowest. This indicates that the formation of an Fe heterostructure can significantly accelerate lithium-ion transport. Consequently, a greater number of lithium ions can be transferred at the negative electrode. It can be inferred that the introduction of SiO_x/Fe@C effectively optimizes and reduces the migration barrier of the Li^+ diffusion path at the interface. Moreover, a comparison of the three SiO_x/C heterostructures reveals that, under identical computational conditions, the energy barrier for lithium-ion migration in SiO_x/C without any metal is 6.19 eV, significantly higher than that in SiO_x/M@C (M = Fe, Co, Ni).[49] This indicates that incorporating metals into the bilayer heterostructure notably lowers the energy barrier for lithium-ion migration.

Adsorption energies

It is worth noting that the influence of individual metals on the migration energy barrier of lithium ions is also reflected in the thermodynamic adsorption energy. The calculated adsorption energies are presented in Tables S1 and 2,† with the values of E(Li + SiO_x/M@C), E(SiO_x/M@C), and E(Li) provided therein. The adsorption energy was calculated using eqn (3):

$$\Delta E_a = E(\mathrm{Li} + \mathrm{SiO}_x/\mathrm{M@C}) - E(\mathrm{SiO}_x/\mathrm{M@C}) - E(\mathrm{Li}) \quad (3)$$

where E(Li + SiO_x/M@C) is the total energy of lithium-ion adsorbed in SiO_x/M@C (M = Fe, Co, Ni), E(SiO_x/M@C) is the total energy of SiO_x/M@C (M = Fe, Co, Ni), and E(Li) is the total energy of a lithium-ion. The adsorption energies of the three materials in all directions are shown in Table 1. Compared with SiO_x/Co@C and SiO_x/Ni@C, lithium ions in SiO_x/Fe@C tend to move towards the center of SiO_x, where the adsorption sites are more stable, and the adsorption energy at each site is relatively uniform. For SiO_x/Co@C, the adsorption energies at the Si_{II} and Si_{III} sites are similar, whereas in SiO_x/Ni@C, the Si_I and Si_{II} sites have similar adsorption energies, as do the Si_{III} and Si_{IV} sites. This variation may be related to the distribution of the metals within the structure.

Considering the average adsorption energies at the four Si sites, SiO_x/Ni@C (2.629 eV) exhibited greater lithium adsorption energy than SiO_x/Co@C (2.402 eV), SiO_x/Fe@C (2.411 eV), showing a stronger Li^+ adsorption capacity. However, it can be found from the migration barrier that Li has the highest energy barrier required in SiO_x/Ni@C. It can be seen that the appropriate adsorption energy is not only conducive to the adsorption of Li without damaging the material structure, but also conducive to the desorption of Li, thereby improving the cycling performance and rate performance. This observation aligns with the lithium-ion adsorption energies observed in MCo_2O_4 (M = Zn, Ni, Cu) system.[62] The average adsorption energies for lithium ions in different metal directions follow a similar pattern: SiO_x/Ni@C (2.442 eV) > SiO_x/Co@C (2.408 eV) > SiO_x/Fe@C (2.302 eV). Given that lithium ions migrate internally and combine with SiO_x, excessive adsorption energy can hinder their migration, thus not facilitating optimal lithium-ion diffusion. Consequently, considering both migration and adsorption energies, SiO_x/Fe@C demonstrates the most favorable performance for lithium-ion transport.

Table 1 The Li^+ adsorption energy for the SiO_x/M@C (M = Fe, Co, Ni)

Material	Direction	ΔE_a/eV	Direction	ΔE_a/eV
SiO_x/Fe@C	Si_I	−2.399936	Fe_I	−2.362536
	Si_{II}	−2.409436	Fe_{II}	−2.093936
	Si_{III}	−2.399836	Fe_{III}	−2.374836
	Si_{IV}	−2.400536	Fe_{IV}	−2.374836
SiO_x/Co@C	Si_I	−2.437436	Co_I	−2.408836
	Si_{II}	−2.531936	Co_{II}	−2.408936
	Si_{III}	−2.531436	Co_{III}	−2.409136
	Si_{IV}	−2.144336	Co_{IV}	−2.407036
SiO_x/Ni@C	Si_I	−2.820136	Ni_I	−2.282936
	Si_{II}	−2.707636	Ni_{II}	−2.499136
	Si_{III}	−2.487836	Ni_{III}	−2.487136
	Si_{IV}	−2.498436	Ni_{IV}	−2.498736

Electronic structure

Through the calculation of the charge density difference, the influence of different metals on charge transfer behavior was elucidated. As illustrated in Fig. 6, the yellow areas indicate charge accumulation while the green areas represent electron depletion. When lithium is inserted between the SiO_x and carbon layers, a significant electron cloud overlap occurs between lithium and silicon atoms, depleting the charge between silicon and oxygen atoms. This phenomenon suggests that lithium adsorption weakens the silicon–oxygen bond interaction, driving the silica conversion reaction. In SiO_x/Fe@C materials, the electron distribution changes over a larger region of the system compared to SiO_x/Co@C and SiO_x/Ni@C. The presence of Fe results in a lower charge density between silicon and oxygen atoms and a higher electron density between lithium and silicon atoms, indicating strong chemical bonds or interactions.

To study the interfacial behavior of heterogeneous nanocrystalline structures during operation, the Fermi energy levels and work functions of carbon, metal, and SiO_x models were calculated, resulting in the energy band diagrams shown in Fig. 7. These diagrams help explain the superior electrochemical properties of different metal heterostructures. In the absence of contact, the Fermi levels of carbon is −2.93 eV, and SiO_x are −0.98 eV, which are higher than those of Fe (−6.54 eV), Co (−4.72 eV), and Ni (−4.02 eV). Due to the differences in Fermi levels between the two phases, charge transfer occurs at the interface, leading to a convergence of Fermi levels.[65,66] Consequently, electrons in carbon transfer to the metal electrode surface, causing negative charge accumulation on the metal side and positive charge on the carbon side, creating an internal electric field from carbon to the metal.

When lithium enters the interface between carbon and the metal, the low electrostatic potential on the metal side attracts lithium ions from the carbon side, neutralizing the accumulated negative charge. Despite the eventual disappearance of the interfacial electric field due to charge equilibrium, the high concentration gradient drives the movement of lithium ions, enhancing their movement towards the SiO_x side and achieving superior conversion reaction kinetics. The largest

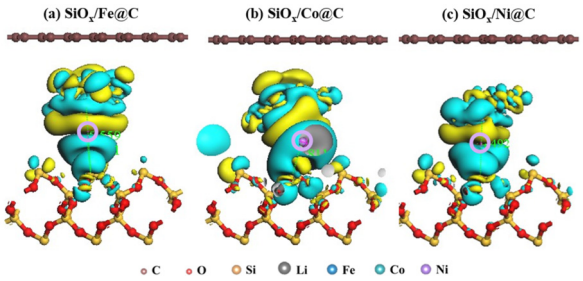

Fig. 6 The charge density distribution for (a) SiO_x/Fe@C; (b) SiO_x/Co@C; (c) SiO_x/Ni@C.

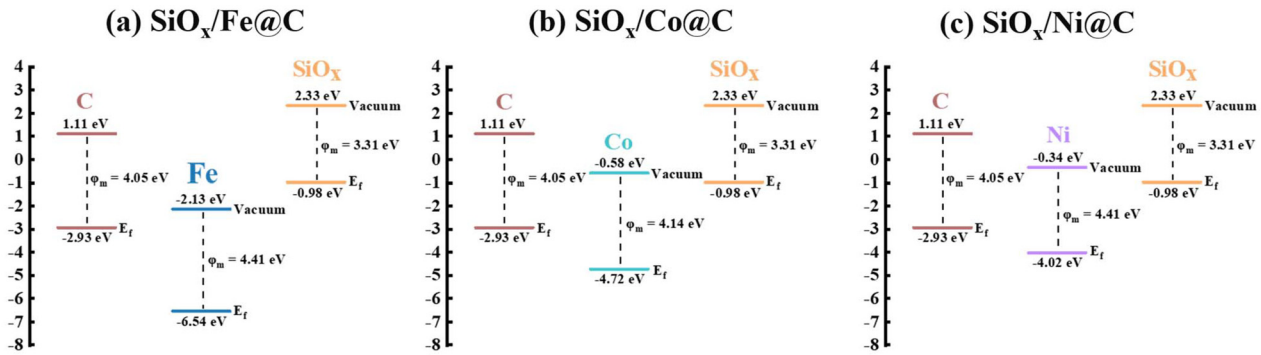

Fig. 7 The Fermi energy levels and work functions for (a) SiO_x/Fe@C; (b) SiO_x/Co@C; (c) SiO_x/Ni@C.

Fermi level difference between Fe and carbon results in the strongest internal electric field, leading to the greatest accumulation of lithium ions, which accelerates interfacial charge transfer and enhances lithium-ion diffusion and rate performance.

Electrochemical properties

To better compare the lithium storage capacities of the three materials, Fe, Co, and Ni-based samples were prepared for electrochemical testing. The rate performance of the silicon oxide composites was evaluated by incrementally increasing the current density (0.1 to 2 A g^{-1}), as depicted in Fig. 8a–c. The SiO_x/Fe@C electrode exhibited superior high-rate performance compared to the other two materials, with discharge capacities of 581.8, 508.8, 471.6, 427.0, and 411.7 mA h g^{-1} at current densities of 100, 200, 500, 1000, and 1500 mA g^{-1}, respectively. At a high current density of 2000 mA g^{-1}, the SiO_x/Fe@C maintained an impressive discharge capacity of 401.9 mA h g^{-1}, outperforming SiO_x/Co@C (124.3 mA h g^{-1}) and SiO_x/Ni@C (52 mA h g^{-1}). When the current density was returned to 100 mA g^{-1}, the capacity recovered to 696.5 mA h g^{-1}, indicating that Fe nanoparticles significantly enhance the

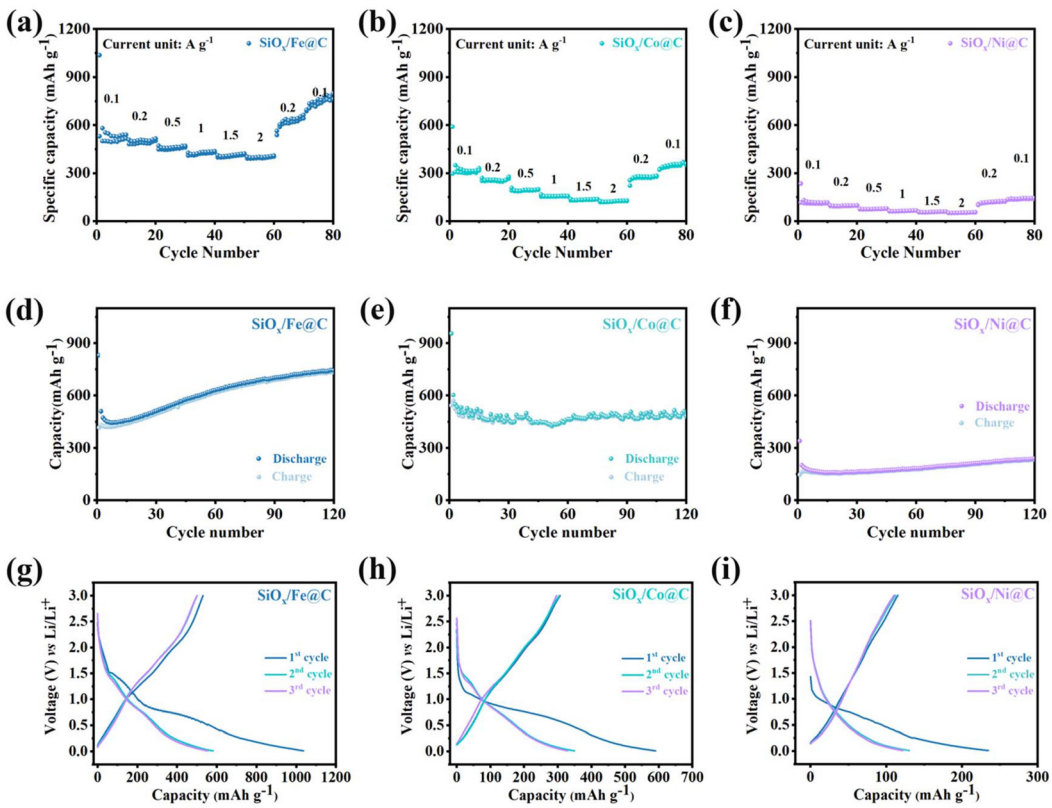

Fig. 8 Rate capability at different current densities from 0.1 to 2 A g^{-1} for (a) SiO_x/Fe@C; (b) SiO_x/Co@C; (c) SiO_x/Ni@C; cycling performance at 0.1 A g^{-1} for (d) SiO_x/Fe@C; (e) SiO_x/Co@C; (f) SiO_x/Ni@C; current charge/discharge (GCD) curves of (g) SiO_x/Fe@C; (h) SiO_x/Co@C; (i) SiO_x/Ni@C.

reversible lithium storage performance of silicon oxide compared to Co and Ni. As shown in Fig. 8d–f, after 120 cycles at a current density of 0.1 A g^{-1}, the reversible capacities of SiO_x/Fe@C, SiO_x/Co@C, and SiO_x/Ni@C were 744.2, 482.4, and 239.6 mA h g^{-1}, respectively. These results demonstrate that conductive Fe nanoparticles enhance ion diffusion kinetics and significantly improve the reversibility and rate capability of the electrode reactions.

Additionally, as observed from the charge–discharge curves for the first three cycles (Fig. 8g–i), the capacity of SiO_x/Fe@C initially reaches 1036.6 mA h g^{-1} after the first cycle but decreases to 581.8 mA h g^{-1} after the second cycle. Similarly, the GCD curves for SiO_x/Co@C (Fig. 8h) and SiO_x/Ni@C (Fig. 8i) exhibit an increase in capacitance during the first cycle followed by a significant decrease in the second cycle. This sharp decline in capacity is primarily attributed to the formation of the solid electrolyte interphase (SEI) layer and the degradation of the electrolyte.[67]

Conclusions

In summary, we have successfully constructed and optimized the SiO_x/M@C (M = Fe, Co, Ni) heterostructures, integrating transition metal nanoparticles (Fe, Co, Ni) into silicon oxide composites. This study thoroughly explores the effects of different metal atoms on SiO_x/C electrodes to address the electrochemical inertness and slow diffusion kinetics of pristine SiO_x. Density Functional Theory (DFT) results and experimental data reveal that the Fe heterostructure exhibits the lowest migration energy barrier, significantly enhancing lithium-ion transport compared to Co and Ni. Consequently, the SiO_x/Fe@C electrode demonstrates superior high-rate discharge capability and excellent cycling performance. The charge density difference calculations underscore the strong electronic interactions and efficient charge transfer behaviors within the SiO_x/Fe@C system, further confirming the enhanced electrochemical properties. Additionally, Fermi level calculations reveal that metal surfaces with greater differences from the Fermi levels of C and SiO_x can accumulate more lithium ions, thereby promoting lithium-ion migration. This study provides a theoretical foundation for the design of advanced silica materials and offers valuable insights into the significance of hybrid strategies for integrating inert metals into anode materials for lithium-ion batteries.

Author contributions

Mianying Huang: conceptualization, formal analysis, writing – original draft, writing–review & editing. Yueying Chen: methodology, resources, formal analysis, writing – review & editing. Wenhai Zeng: conceptualization. Yiqing Liu: investigation. Zhiguang Xu: conceptualization, writing – review & editing, supervision. Yongbo Wu: conceptualization. Xiaoming Lin: conceptualization, writing – review & editing, supervision. Xuan Xu: conceptualization, writing – review & editing.

Data availability

Data will be made available on request.

Conflicts of interest

The authors declare that they have no known competing financial interests or personal relationships that could have appeared to influence the work reported in this paper.

Acknowledgements

This work was financially supported by Open Fund of Energy and Materials Chemistry Joint Laboratory of SCNU and TINCI, China (SCNU-TINCI-202207). Furthermore, the authors would like to thank the Shiyanjia lab (**https://www.shiyanjia.com**).

References

1 X. Han, Y. Liang, L. Zhao, J. Wang, Q. Xia, D. Li, Y. Liu, Z. Zhou, Y. Long and Y. Li, *Mater. Futures*, 2022, **1**, 035102.
2 R. Shi, S. Jiao, Q. Yue, G. Gu, K. Zhang and Y. Zhao, *Exploration*, 2022, **2**, 20220066.
3 S. Li, K. Wang, G. Zhang, S. Li, Y. Xu, X. Zhang, X. Zhang, S. Zheng, X. Sun and Y. Ma, *Adv. Funct. Mater.*, 2022, **32**, 2200796.
4 W. Cheng, M. Zhao, Y. Lai, X. Wang, H. Liu, P. Xiao, G. Mo, B. Liu and Y. Liu, *Exploration*, 2024, **4**, 20230056.
5 Y. Chen, T. Wang, H. Tian, D. Su, Q. Zhang and G. Wang, *Adv. Mater.*, 2021, **33**, 2003666.
6 Z. Hui, J. An, J. Zhou, W. Huang and G. Sun, *Exploration*, 2022, **2**, 20210237.
7 L. Ben, J. Zhou, H. Ji, H. Yu, W. Zhao and X. Huang, *Mater. Futures*, 2021, **1**, 015101.
8 M. Qi, L. Wang, X. Huang, M. Ma and X. He, *Small*, 2024, 2402443.
9 T. L. Kulova, V. N. Fateev, E. A. Seregina and A. S. Grigoriev, *Int. J. Electrochem. Sci.*, 2020, **15**, 7242–7259.
10 J. Ren, Z. Wang, P. Xu, C. Wang, F. Gao, D. Zhao, S. Liu, H. Yang, D. Wang and C. Niu, *Nano-Micro Lett.*, 2022, **14**, 1–14.
11 L. Zhang, X. Li, M. Yang and W. Chen, *Energy Storage Mater.*, 2021, **41**, 522–545.
12 C. Tian, Q. Qin and L. Suo, *Mater. Futures*, 2023, **2**, 012101.
13 Z. Shang, W. Yu, J. Zhou, X. Zhou, Z. Zeng, R. Tursun, X. Liu and S. Xu, *eTransportation*, 2024, **20**, 100320.
14 H. Chang, Y. R. Wu, X. Han and T. F. Yi, *Energ. Mater.*, 2021, **1**, 100003.
15 J. Liu, B. Li, J. Cao, X. Xing and G. Cui, *J. Energy Chem.*, 2024, **91**, 73–98.
16 M. Jiao, Y. Wang, C. Ye, C. Wang, W. Zhang and C. Liang, *J. Alloys Compd.*, 2020, **842**, 155774.
17 M. Winter, *Adv. Mater.*, 1998, **10**, 725–763.

18 D. Zhang, J. Ren, C. Li, B. Luo, L. Wang and Y. Li, *Chin. J. Struct. Chem.*, 2022, **41**, 2205055–2205062.
19 J. Zhao, B. Wang, Z. Zhan, M. Hu, F. Cai, K. Świerczek, K. Yang, J. Ren, Z. Guo and Z. Wang, *J. Colloid Interface Sci.*, 2024, **664**, 790–800.
20 L. Zhang, C. Wang, Y. Dou, N. Cheng, D. Cui, Y. Du, P. Liu, M. Al-Mamun, S. Zhang and H. Zhao, *Angew. Chem., Int. Ed.*, 2019, **58**, 8824–8828.
21 A. Franco Gonzalez, N. H. Yang and R. S. Liu, *J. Phys. Chem. C*, 2017, **121**, 27775–27787.
22 Y. F. Yang, J. L. Yang, F. Pan and Y. Cui, *Chin. J. Struct. Chem.*, 2020, **39**, 2011–2715.
23 P. Zhang, X. Wang, Y. Zhang, Y. Wei, N. Shen, S. Chen and B. Xu, *Adv. Funct. Mater.*, 2024, 2402307.
24 L. Sun, Y. Liu, L. Wang and Z. Jin, *Adv. Funct. Mater.*, 2024, 2403032.
25 S. Chen, X. Li, C. W. Kao, T. Luo, K. Chen, J. Fu, C. Ma, H. Li, M. Li and T. S. Chan, *Angew. Chem., Int. Ed.*, 2022, **61**, e202206233.
26 Y. Jiang, J. Wen, Z. Ding, Y. Ren, Z. Liu, X. Chen and X. Zhou, *J. Alloys Compd.*, 2021, **861**, 157932.
27 F. Wan, W. Wang, Z. Zou, H. Xie, H. Ping and Z. Fu, *J. Mater. Sci. Technol.*, 2021, **72**, 61–68.
28 Z. Li, M. Han, P. Yu, J. Lin and J. Yu, *Nano-Micro Lett.*, 2024, **16**, 98.
29 Q. Xu, J. K. Sun, Y. X. Yin and Y. G. Guo, *Adv. Funct. Mater.*, 2018, **28**, 1705235.
30 T. Shang, Y. Wen, D. Xiao, L. Gu, Y. S. Hu and H. Li, *Adv. Energy Mater.*, 2017, **7**, 1700709.
31 Y. Gao, R. Yi, Y. C. Li, J. Song, S. Chen, Q. Huang, T. E. Mallouk and D. Wang, *J. Am. Chem. Soc.*, 2017, **139**, 17359–17367.
32 S. Fu, X. Wang, F. Yao, Q. He, F. Xie, X. Wu, S. Tong and M. Wu, *Chem. Eng. J.*, 2024, **489**, 151151.
33 Y. Shen, Z. Cao, Y. Wu, Y. Cheng, H. Xue, Y. Zou, G. Liu, D. Yin, L. Cavallo and L. Wang, *J. Mater. Chem. A*, 2020, **8**, 12306–12313.
34 G. Zhu, D. Chao, W. Xu, M. Wu and H. Zhang, *ACS Nano*, 2021, **15**, 15567–15593.
35 J. Y. Li, G. Li, J. Zhang, Y. X. Yin, F. S. Yue, Q. Xu and Y. G. Guo, *ACS Appl. Mater. Interfaces*, 2019, **11**, 4057–4064.
36 L. Sun, Y. Liu, R. Shao, J. Wu, R. Jiang and Z. Jin, *Energy Storage Mater.*, 2022, **46**, 482–502.
37 Z. Liu, D. Guan, Q. Yu, L. Xu, Z. Zhuang, T. Zhu, D. Zhao, L. Zhou and L. Mai, *Energy Stor. Mater.*, 2018, **13**, 112–118.
38 Z. Gu, X. Xia, C. Liu, X. Hu, Y. Chen, Z. Wang and H. Liu, *J. Alloys Compd.*, 2018, **757**, 265–272.
39 Z. Liu, Y. Zhao, R. He, W. Luo, J. Meng, Q. Yu, D. Zhao, L. Zhou and L. Mai, *Energy Storage Mater.*, 2019, **19**, 299–305.
40 T. Luo, H. Jiang, Z. Qing, Z. Zhang, L. Li and D. Fang, *ChemPlusChem*, 2024, e202400240.
41 J. Xiong, Q. Li, X. Tan, X. Guo, K. Li, Q. Luo, Y. Chen, X. Tong, B. Na and M. Zhong, *Dalton Trans.*, 2024, **53**, 11232–11236.
42 S. Ji, R. Song, H. Yuan, D. Lv, L. Yang, J. Luan, D. Wan, J. Liu and C. Zhong, *J. Electroanal. Chem.*, 2024, **959**, 118141.
43 X. Xue, X. Liu, B. Lou, Y. Yang, N. Shi, F. Wen, X. Yang and D. Liu, *J. Energy Chem.*, 2023, **84**, 292–302.
44 K. Wang, X. Zhu, Y. Hu, S. Qiu, L. Gu, C. Wang and P. Zuo, *Carbon*, 2020, **167**, 835–842.
45 A. Belgibayeva, Z. Kawate and I. Taniguchi, *Mater. Lett.*, 2021, **291**, 129595.
46 X. Wang, S. Tang, W. Guo, Y. Fu and A. Manthiram, *Mater. Today*, 2021, **50**, 259–275.
47 B. Bai, L. Qiu, Y. Liu, Z. Su, L. Song and P. Du, *J. Mater. Chem. C*, 2023, **11**, 13466–13475.
48 Q. Zhong, K. Zhou, Z. Yang and J. Yu, *J. Energy Storage*, 2024, **97**, 112784.
49 Y. Chen, M. Huang, G. Deng, C. Wu, H. Zhong, A. Zeb, X. Lin, Y. Wu, Z. Wu and Z. Xu, *Chem. Eng. J.*, 2024, **486**, 150111.
50 T. Liang, R. Hu, H. Zhang, H. Zhang, H. Wang, Y. Ouyang, J. Liu, L. Yang and M. Zhu, *J. Mater. Chem. A*, 2018, **6**, 7206–7220.
51 X. Zhao, Y. Liu, Y. Zhang, Q. Lu, T. Gao, M. Su, X. Li and Y. Liu, *Funct. Mater. Lett.*, 2024, **17**, 2451017.
52 J. Sun, H. Zhou and Z. Huang, *Green Chem.*, 2024, **4**, 4.
53 C. Yang, Y. Hao, J. Wang, M. Zhang, L. Song and J. Qu, *Front. Chem.*, 2024, **12**, 1400758.
54 J. Zhou, C. Xing, J. Huang, Y. Zhang, G. Li, L. Chen, S. Tao, Z. Yang, G. Wang and L. Fei, *Adv. Energy Mater.*, 2024, **14**, 2302761.
55 M. Huang, Z. Xu and X. Lin, *Chin. J. Struct. Chem.*, 2024, 100309.
56 A. Xu, M. Huang, C. Liu, T. Li, X. Li, S. Wu, Z. Xu and Y. Yan, *Adv. Funct. Mater.*, 2024, 2400302.
57 Y. Chen, P. Li, M. Huang, C. Wu, Q. Huang, T. Xie, X. Lin, A. Zeb, Y. Wu and Z. Xu, *J. Energy Chem.*, 2024, **98**, 180–189.
58 H. Ou, M. Huang, P. Li, C. Jiang, H. Zhong, Z. Wu, M. Zhao, X. Lin, A. Zeb and Y. Wu, *J. Colloid Interface Sci.*, 2024, **672**, 753–764.
59 G. Ou, M. Huang, X. Lu, I. Manke, C. Yang, J. Qian, X. Lin and R. Chen, *Small*, 2024, **20**, 2307615.
60 X. Zhang, M. Huang, Z. Peng, X. Sang, Y. Liu, X. Xu, Z. Xu, A. Zeb, Y. Wu and X. Lin, *J. Colloid Interface Sci.*, 2023, **652**, 1394–1404.
61 S. J. Clark, M. D. Segall, C. J. Pickard, P. J. Hasnip, M. I. Probert, K. Refson and M. C. Payne, *Z. Kristallogr. - Cryst. Mater.*, 2005, **220**, 567–570.
62 Y. Guo, M. Huang, H. Zhong, Z. Xu, Q. Ye, J. Huang, G. Ma, Z. Xu, A. Zeb and X. Lin, *J. Colloid Interface Sci.*, 2023, **650**, 1638–1647.
63 X. Zhang, G. Deng, M. Huang, Z. Xu, J. Huang, X. Xu, Z. Xu, M. Li, L. Hu and X. Lin, *J. Energy Chem.*, 2024, **88**, 112–124.
64 N. L. Allinger, X. Zhou and J. Bergsma, *J. Mol. Struct.: THEOCHEM*, 1994, **312**, 69–83.
65 S. Wu, Q. Yang, Z. Zhang and W. He, *Surf. Interfaces*, 2022, **29**, 101789.
66 L. Fang, Z. Lan, W. Guan, P. Zhou, N. Bahlawane, W. Sun, Y. Lu, C. Liang, M. Yan and Y. Jiang, *Energy Storage Mater.*, 2019, **18**, 107–113.
67 Y. S. Choi, W. Choi, W. S. Yoon and J. M. Kim, *ACS Nano*, 2022, **16**, 631–642.

